Research article

Fundamental investigation of photoacoustic signal generation from single aerosol particles at varying relative humidity

Matus E. Diveky[1], Sandra Roy[1], Grégory David, Johannes W. Cremer, Ruth Signorell*

Laboratory of Physical Chemistry, Department of Chemistry and Applied Biosciences, ETH Zürich, Vladimir-Prelog-Weg 2, CH-8093 Zürich, Switzerland

ABSTRACT

Photoacoustic (PA) spectroscopy enjoys widespread applications across atmospheric sciences. However, experimental biases and limitations originating from environmental conditions and particle size distributions are not fully understood. Here, we combine single-particle photoacoustics with modulated Mie scattering to unravel the fundamental physical processes occurring during PA measurements on aerosols. We perform measurements on optically trapped droplets of varying sizes at different relative humidity. Our recently developed technique – photothermal single-particle spectroscopy (PSPS) – enables fundamental investigations of the interplay between the heat flux and mass flux from single aerosol particles. We find that the PA phase is more sensitive to water uptake by aerosol particles than the PA amplitude. We present results from a model of the PA phase, which sheds further light onto the dependence of the PA phase on the mass flux phenomena. The presented work provides fundamental insights into photoacoustic signal generation of aerosol particles.

1. Introduction

Photoacoustic (PA) spectroscopy is a highly sensitive light absorption technique that is used across a wide spectrum of scientific disciplines, such as biology [1,2], material sciences [3,4], medicine [5,6] and atmospheric sciences [7,8]. PA spectroscopy measures light absorption directly and hence is widely used for trace gas analysis [9–16] and aerosol absorption measurements [17–27]. Optical properties of aerosols, such as their absorption of sunlight, are of crucial importance for accurate global climate modelling due to the ubiquitous nature of aerosols in the atmosphere and their strong influence on the climate through a combination of direct and indirect effects [28–30].

Several field campaigns used PA spectroscopy to measure absorption of atmospheric aerosol ensembles [20,22–24,31]. Such *in situ* absorption studies are of a great importance for the vertical profiling of aerosol absorption, which is essential for the calculations of the radiative impact of aerosols [32]. However, there are several limitations and biases associated with PA aerosol measurements. For a better understanding of these limiting factors, fundamental studies are crucial in order to unravel the governing phenomena behind the PA signal generation from aerosols. One way to perform controlled experiments is to study single particles as opposed to ensembles. Experiments on single particles allow one to control the particle size, composition and environmental conditions (temperature and relative humidity) while avoiding the averaging effects present in ensemble measurements [33–38].

Recently, various single-particle studies have been carried out across different scientific fields in order to assess physical properties of aerosols under controlled conditions [38–44]. Optical traps are often used to isolate single aerosols as they afford a good spatial confinement, don't induce any structural or composition changes to the particles, enable multiple measurements to be performed simultaneously in custom-built cells at ambient conditions and can be used for trapping differently sized particles [45]. In our previous work, we developed the first single-particle PA spectrometer [46], with which we were able to experimentally observe nanofocusing of light inside a trapped particle [46], measure the theoretically predicted size-dependent damping of the PA signal [47,48] and, in our most recent work, retrieve the mass accommodation coefficient of water on miscible organic aerosols at different particle temperatures and concentrations [49].

Environmental conditions, such as relative humidity, influence the optical properties of atmospheric aerosols and hence their impact on the climate. For example, in the areas of high relative humidity (RH), an uptake of water by aerosols affects their scattering and absorption properties [50–52]. Ensemble PA spectroscopy has been used in the past to investigate the RH dependence of aerosols' absorption, however

the results of these studies remained inconsistent. Some studies suggested that the PA signal decreased with increasing RH [31,53,54], while a different study observed an increase in the PA signal with increasing RH [55]. These RH-trends originate either from a change in the absorptive properties of aerosols at elevated RH or from an experimental bias that influences the PA signal generation at elevated RH. In order to shed light onto the fundamental processes governing the RH dependence of the PA signal, we decided to perform single-particle PA measurements at varying RH [56]. In this previous work, we found evidence suggesting that the RH-dependence of the PA amplitude (PAA) was a function of particle size – an effect we attributed to the interplay between the heat flux and mass flux contributions to the overall PA signal.

The PA signal provides two measurable quantities – the PAA and the PA phase (PAP) – both of which carry unique information about the system under investigation. The PAP is used across disciplines, for example to measure tissue elasticity [57], to improve biomedical imaging techniques [58], to study ripening of papayas [2] or to perform depth-resolved analysis [59]. In atmospheric sciences, contaminants can be identified using the PAP [9] while high-sensitivity aerosol absorption measurements also require the evaluation of the PAP component [17]. In a recent laboratory study [49], we have employed the PAP to determine the mass accommodation coefficient of water on organic aerosol particles.

The inherent physical processes accompanying any PA measurement of liquid aerosols include an oscillatory size change of the particle occurring at the modulation frequency of the excitation laser. This size change is a result of coupled effects of heat expansion and mass flux. The exquisite dependence of elastic light scattering on the size of spherical particles (Mie scattering) allows for the experimental retrieval of such size changes accompanying the PA signal generation process [56]. Such photothermal tuning of Mie scattered light dates back to the 1980s [60–63], when it was used to perform the first ever single particle light absorption measurement [64]. The so-called modulated Mie scattering (MMS) shows a very high sensitivity to even sub-nanometre size changes so that Arnold et al. were able to retrieve particle size changes of 0.1 nm [65]. More recently, a fully reversible 40 nm size change of salt droplets was induced by photothermal tuning [66]. Such sensitive scattering technique proved invaluable for our purpose to unravel the various phenomena that contribute to the PA signal generation.

In the present work, we employ our recently developed technique [49] – photothermal single-particle spectroscopy (PSPS) – that combines simultaneous single-particle photoacoustic and scattering measurements in order to investigate fundamental physical processes inherent to any PA measurement of aerosols. The underlying phenomena that describes the PSPS technique is an oscillatory temperature change of the particle induced by the intensity modulated excitation laser. Such oscillatory temperature change results in a photoacoustic effect as well as in a periodic perturbation of the scattering profile of the particle. The experimental data set presented has been used previously to retrieve the mass accommodation coefficient of water on mixed organic-water droplets [49], and for the analysis of the RH dependence of the PAA [56]. Here, we focus our analysis of the PA signal generation on its PAP component. We analyse the dependence of PAP and MMS on the RH, and we use the MMS data recorded at different relative humidities and for different particle sizes to infer the changes of droplet size and water concentration of the particle during one PA cycle. Using the MMS as an independent probe, we further analyse and discuss the PA signal contributions arising from the heat and mass flux and from the volume change of the particle itself. We support our measurements with a thorough analysis of simulations which show good agreement with the experiment.
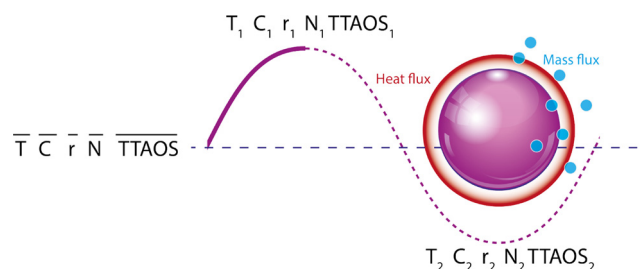

Fig. 1. A depiction of a PA process originating from an aerosol particle (purple sphere). An intensity modulated excitation laser induces periodic heating and cooling of the particle resulting in a pressure wave (sound wave) formation in the surrounding air. The energy exchange between the particle and the surrounding gas happens through the mass and heat flux, both of which contribute to the PA signal. The particle's temperature (T), concentration (C), radius (r), complex refractive index (N) and the integrated scattered light by the particle (TTAOS) vary during one PA cycle. The corresponding average properties are denoted by a bar, e.g. $\bar{T}$ for the average particle temperature, while the properties at the elevated temperature are denoted with a subscript 1 and the properties at the reduced temperature with a subscript 2.

2. Experimental

2.1. Photoacoustics and modulated Mie scattering

In single particle photoacoustics, the irradiation of an aerosol particle in a resonant PA cell with an intensity modulated laser leads to modulated light absorption, which in turn alters the temperature of the particle. Such a cyclic temperature variation (at the modulation frequency of the laser) leads to fast energy exchange between the particle and the surrounding gas [67] through either mass flux (I) or heat flux (Q), or both. The heat flux represents the direct heat exchange between the particle and the surrounding gas through collisions. The mass flux arises from periodic condensation and evaporation of volatile species (in the present study water) onto and from the particle (see Fig. 1). Both pathways contribute to the heat dissipation (the mass flux through latent heat) and give rise to a pressure wave, i.e. a sound wave, that is detected using a microphone. The PA signal is composed of two components, its amplitude and its phase.

The PA process also induces oscillations of the particle size through heat expansion and mass flux. The fluctuations in temperature cause the particle to expand and contract (heat expansion) while the water transfer (mass flux) changes the size of the particle by changing its mass and composition (Fig. 1). This particle size change can be accessed experimentally by monitoring the elastically scattered light from the particle using a photodiode (Hamamatsu, S2506-02). Integrating the scattering signal over a certain solid angle (the collection angle) yields the total two-dimensional angular optical scattering (TTAOS) signal [49]. The TTAOS depends on the properties of the trapped aerosol particle, such as its size and refractive index, and exhibits characteristic Mie resonances at specific particle sizes (Fig. 2 blue). The above-mentioned oscillations of the particle's size (and composition) modulate the scattered light. The resulting minute oscillatory component of the TTAOS signal constitutes the MMS signal. Analogous to the PA signal, MMS has both an amplitude and phase component. Its amplitude (MMS$_A$, Fig. 2 red) is determined by the change of the particle's properties (refractive index and size) in the course of the PA cycle and is therefore correlated to the slope of the TTAOS signal. This leads to sharp double-peak features in the MMS$_A$ whenever the TTAOS passes through a Mie resonance (Fig. 2). The phase of the MMS signal (MMS$_P$) originates from the time delay between the PA laser emission and the scattered light detection. MMS$_P$ (Fig. 2 orange) shifts by 180° as the slope of the TTAOS signal changes sign.
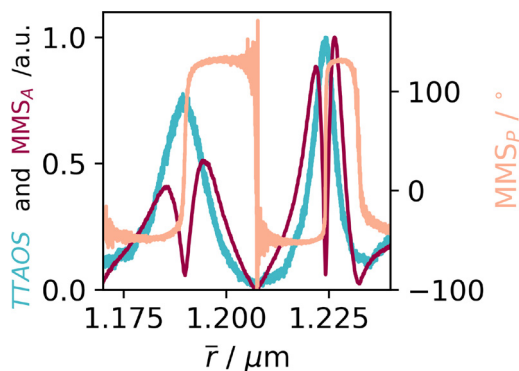
Fig. 2. An example of two experimental Mie resonances in the TTAOS signal (blue), with the corresponding MMS_A (red) and MMS_P (orange) as a function of the droplet average radius $\bar{r}$.

2.2. Experimental setup

Single particle experiments were realised by isolating single aerosol droplets inside the resonant PA cell using counter-propagating optical tweezers. The experimental set up is presented in details in Ref. [56] (Fig. 2) and in Ref. [49]. A continuous visible laser (Laser Quantum, Opus 532, 532 nm), linearly polarised at 45° was directed towards a polarisation beamsplitter cube, creating two beams of equal intensity. Both beams were then redirected in a counter-propagating configuration and focused at same point in space, where a single aerosol droplet is trapped by optical forces. A proportional-integral-derivative (PID) controller with a 4 kHz frequency response was used to optimise the power of the two trapping beams in order to ensure a stable position of the particle in the optical trap. This feedback stabilisation was achieved through projecting visible light elastically scattered from the trapped particle onto a quadrant photodiode (Hamamatsu, S5980) and changing the polarisation of the incident trapping laser beam using an electro-optic modulator [49,56].

Measurements were performed in a specially designed resonant PA cell [25,46,68]. The cell contains a 4 cm long acoustic resonator (4 mm diameter) to enhance the PA signal induced by the intensity modulated IR laser (referred to as the PA laser) at 4 kHz (AdTech Optics, 9.47 μm diode laser). The laser diode was mounted in a C-mount laser mount (LDMC20, Thorlabs) and the laser emission was collimated using a moulded IR aspheric lens (C036TME-F, Thorlabs). The collimated PA laser was directed using silver mirrors onto a ZnSe lens (75.0 mm, LA7660-G, Thorlabs) which focused the light onto the particle. Two buffer volumes are located at either side of the acoustic resonator to minimise outside noise. The gas inlet and outlet located in one of the buffer volumes were used to control the RH between 11% and 93% by a constant flow of humidified nitrogen gas inside the cell. Since the gas inlet and outlet are located in the same buffer volume, the trapped particle does not get affected by a direct gas flow. Diffusion through the cell allowed for a relative humidity equilibrium to be reached, which was monitored with a RH and temperature sensor placed in the opposite buffer volume. The counter-propagating tweezers entered the PA cell perpendicular to the PA resonator through BK7 glass windows, while the PA laser passed through the cell parallel to the PA resonator through BaF_2 windows. The PA signal was measured using a microphone (Knowles Electronics, EK-23133-C36) placed underneath the droplet at an antinode of the targeted acoustic mode. The trapping laser was elastically scattered from the particle and the scattered light was collected over an angle of 49.6° at the top of the cell using a microscope objective (Mitutoyo, M Plan Apo 20× Objective) and split to a CMOS camera, a quadrant photodiode (Hamamatsu, S5980) and a photodiode (Hamamatsu, S2506-02). The signal from the CMOS camera was used to visually monitor the droplet, while the signal from the quadrant photodiode was used for feedback stabilisation. The TTAOS signal from the

photodiode was used for particle size fitting [56], while the demodulated TTAOS signal yielded the MMS signal. Both the TTAOS signal and the microphone signal were demodulated at 4 kHz using a lock-in amplifier (Zurich Instruments, 500 kHz MFLI) to retrieve the complex (amplitude and phase) MMS and PA signals, respectively. The reference output of the lock-in amplifier served as modulation reference for the PA laser to assure maximum synchronisation between the driving and measured signals, which is necessary for sensitive phase measurements. The MMS data were recorded concomitantly with the PA data.

Tetraethylene glycol (TEG, Acros Organics) was aerosolised for about 1 s and the flow of aerosols was introduced into the PA cell through the gas inlet located in one of the buffer volumes. The aerosol particles diffuse into the PA resonator where one of them gets trapped with the counter-propagating tweezers. The nitrogen flow is used to remove any remaining aerosol particles from the PA cell leaving only single trapped particle. The trapped particle was left for a few minutes to equilibrate with the humidified nitrogen gas. The equilibrated mixed TEG-water droplets were irradiated with the PA laser. Note that TEG and water are fully miscible. The absorption of the PA laser by TEG raises the particle's average temperature ($\bar{T}$) above that of its surroundings, speeding up the slow evaporation of TEG over the course of the PA measurement (~20 min) [49,56]. The gradual shrinking of the particle allows us to access a wide range of particle sizes (from 3.5 to 0.7 μm in radius) in a single experiment. Note that during a PA cycle (250 μs) only water evaporates significantly, while TEG evaporation can be neglected on this fast time scale as its vapour pressure is seven orders of magnitude smaller than that of water. Over 390 measurements were performed at different initial particle sizes and over a wide range of relative humidities from 11% to 93%. At the end of each measurement, the droplet was removed from the trap, and a PA background measurement was acquired. The complex PA background was subtracted from the PA signal as the background signal was found to have a constant phase (further details in the Supporting Information of Ref. [49]). All the PA data were averaged according to their sizes and relative humidities. Note that our PA set-up does not yield absolute values for the PAA and PAP. Only the relative changes of these values as a function of particle size and relative humidity can be directly compared with the simulation. The MMS signal results from, in principle, a background free measurement, and the background was indeed found to be insignificant.

At the maxima of the Mie resonances in the TTAOS signal (Fig. 2, blue trace), the MMS_A signal (red trace) is characterised by very sharp minima, whose position is limited by the resolution of the size determination of a few nm. Therefore, it would not be useful to average MMS_A traces from different measurements. For the same reason the direct fit of the full traces to the model would not yield satisfactory results. To avoid these issues, we only consider the maxima of the MMS_A traces in the statistical averaging and in the subsequent fit of the MMS_A data. The maxima are determined separately for each measurement with their amplitude normalised to the corresponding value of the TTAOS signal. As illustrated in Fig. 2, the MMS_P (orange trace) undergoes a shift of 180° across the Mie resonances (see Fig. 2 blue) reflecting the change of sign in the slope of the TTAOS signal. To account for this in our analysis, 180° was added to all negative MMS_P values. For additional information see section S1 in the Supplementary Material.

2.3. Model

The model for the PA signal generation presented here is adapted from the work of Murphy [69] and Raspet et al. [70]. Details can be found in Refs. [49,56]. According to this model, the modulated PA laser introduces a small uniform oscillation of the particle temperature ΔT:

$$\Delta T = \frac{I_0 C_{\text{abs}}}{4\pi\bar{r}K\beta_T \, |1 + f_M - i\omega\tau|} \tag{1}$$

where I_0 is the incident light intensity, C_{abs} is the absorption cross

section of the particle, $\bar{r}$ is the particle radius averaged over one PA cycle, K is the heat conductivity of the surrounding gas, β_T is the heat transition flow correction factor, f_M is the ratio of the energies dissipated through mass flux to heat flux, ω is the angular frequency of the PA laser and τ is the thermal response time expressed as:

$$\tau = \frac{r^2 \rho c_p}{3K\beta_T} \tag{2}$$

where ρ is the density of the particle and c_p is the specific heat capacity of the particle. ΔT directly yields the corresponding amplitudes of the heat flux (ΔQ) and mass flux (ΔI) oscillations. Both contribute to the formation of a pressure wave in the surrounding gas phase, adjacent to the particles surface, whose amplitude is proportional to the PA signal S:

$$S = \frac{R}{p}\left(\frac{\Delta Q}{M_g c_{p,g}} + \frac{\Delta I T_\infty}{M_w}\right) \tag{3}$$

where R is the universal gas constant, p is the ambient pressure (1 atm.), M_g is the molar mass of the surrounding gas, $c_{p,g}$ is the heat capacity of the gas, M_w is the molar mass of water and T_∞ is the ambient temperature (293.65 K). The very small contribution of the oscillations of the particle's volume are neglected here (see Section 3.3). The contribution from the heat flux to the PAA signal is defined as:

$$HF = \frac{R\Delta Q}{pM_g c_{p,g}} \tag{4}$$

while the mass flux contribution to the PAA signal is:

$$MF = \frac{R\Delta I T_\infty}{pM_w} \tag{5}$$

The PA signal is a complex quantity with amplitude $|S|$ and phase $\theta(S)$:

$$\theta(S) = \arg\left(\frac{1}{1 + f_M - i\omega\tau}\right) \tag{6}$$

where $arg(y)$ retrieves the argument of a complex number y. Through ΔI and f_M [49,56] both the PAA and PAP depend on the mass accommodation coefficient (α_M), which represents the probability of a gas phase molecule of the volatile particle component (in this case water) to stick to the surface of an aerosol particle upon collision. From the mass flux component, we obtain the amplitude of the oscillation of the water content in the particle, Δn:

$$\Delta n = \frac{\Delta I}{M_w}\Delta t = \frac{4\pi\bar{r}D\beta_M p_v}{RT_\infty \bar{T}}\left(\frac{LM_v}{RT_\infty} - 1\right)\Delta T\Delta t \tag{7}$$

where D is the diffusion constant of water in air, β_M is the mass transition flow correction factor, p_v is the water vapour pressure, $\bar{T}$ is the particle temperature averaged over one PA cycle, L is the latent heat of water, Δt is one quarter of the 4 kHz PA period. The mass transition flow correction factor is defined as:

$$\beta_M = \frac{1 + Kn_M}{1 + \left(\frac{4}{3\alpha_M} + 0.377\right)Kn_M + \frac{4}{3\alpha_M}(Kn_M)^2} \tag{8}$$

where Kn_M is the Knudsen number calculated as:

$$Kn_M = \frac{\lambda_v}{r} \tag{9}$$

where λ_v is the mean free path of water in nitrogen at ambient conditions (102 nm).

The change of particle mass is crucial for modelling of the MMS_A. The change of mass, particle composition and the heat expansion were considered when calculating the variation in the total Mie scattering. The MMS_A is related to the change in the particle TTAOS signal divided by the average TTAOS signal ($T\bar{T}AOS$):

$$MMS_A = \frac{|TTAOS_1 - TTAOS_2|}{T\bar{T}AOS} \tag{10}$$

The TTAOS signal is modelled using Mie theory using the particle size (r) and complex refractive index (N). To calculate the size evolution during a PA cycle, one must take into consideration the density of the particle at its average temperature and water concentration, $\rho(\bar{T}, \bar{C})$, the mass change caused by the evaporation/condensation of water (from $\bar{T}$ to T) as well as the density at its current temperature and concentration, $\rho(T, C)$:

$$r = \left(\frac{3}{4\pi}\left(\underbrace{\frac{4\pi\bar{r}^3}{3}\rho(\bar{T}, \bar{C})}_{\text{mass at } \bar{T}} \pm \underbrace{\Delta n M_w}_{\text{mass change}}\right)\frac{1}{\rho(T, C)}\right)^{1/3} \tag{11}$$

To calculate the complex refractive index of the particle (N), we used the Lorentz-Lorenz approximation as it was shown to be a good approximation for a similar system [71]:

$$\frac{N^2 - 1}{N^2 + 2} = \frac{V_w}{V}\frac{N_w^2 - 1}{N_w^2 + 2} + \frac{V_{TEG}}{V}\frac{N_{TEG}^2 - 1}{N_{TEG}^2 + 2} \tag{12}$$

where N_w and N_{TEG} are the complex refractive index at T of water and TEG respectively, V is the volume of the particle, V_w and V_{TEG} are the volume of water and TEG inside the particle respectively.

The water concentration (C, in % mass) is RH and droplet size dependent (Fig. 3). For all droplet sizes, the water concentration increases with increasing RH, with the increase being the most pronounced at 85% and 93% RH. The water concentration changes with the particle size due to a change in particle average temperature $\bar{T}$, which is higher for larger particle sizes. This is because of larger absorption cross sections for the PA laser at larger particle sizes [49,56]. Fig. 3 illustrates the resulting decrease of water concentration as a function of particle size at all RHs.

3. Results

Fig. 4 shows the experimental PAA and PAP signals that were collected from single optically-trapped TEG-water droplets of different sizes at 29 different relative humidities [49]. The individual curves shown are averages of multiple single-particle measurements at a given RH. Standard deviations were calculated for all averages, but for clarity only average error bars are shown in the plots. The PA signal was modelled as described in Section 2.3. We focus on the analysis of the PAP dependence on RH and droplet size (Section 3.1), as the dependence of PAA on RH and droplet size have been analysed previously [56]. Concomitant MMS measurements performed alongside the PA measurements provide further insight into fundamental physical processes during the PA cycle. The raw MMS data is presented in the
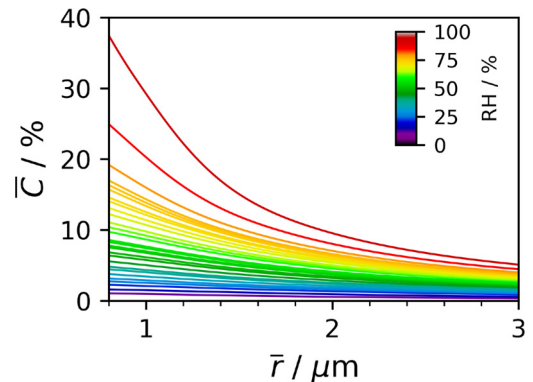
Fig. 3. Calculated water average concentration $\bar{C}$ (in % mass) as a function of the average droplet radius $\bar{r}$ and the relative humidity RH for mixed TEG-water droplets.
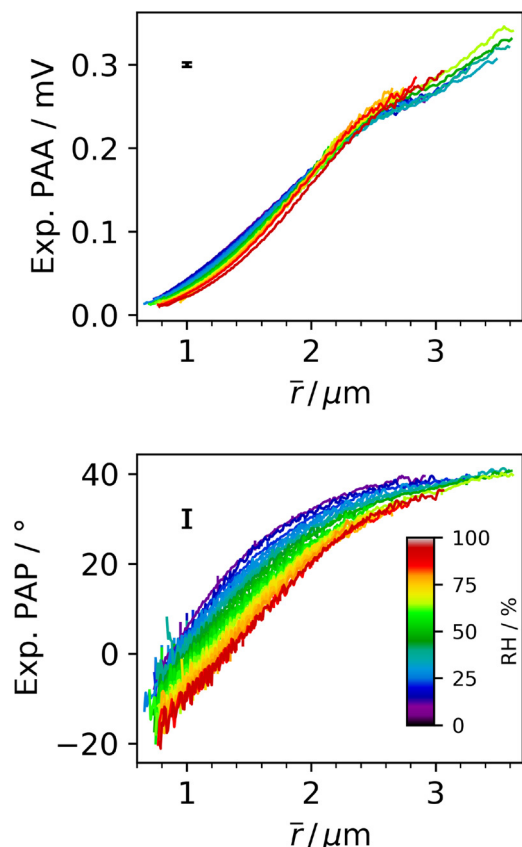
Fig. 4. Experimental PAA (top) and PAP (bottom) as a function of droplet average radius $\bar{r}$ and relative humidity RH [56] for mixed TEG-water droplets. The data shown are averages of single-particle measurements. For clarity purposes, only average error bars are shown. Note that our PA set-up does not yield absolute values for the PAA and PAP (see text).

Supplementary Material, Section S1. Their analysis in Section 3.2 gives access to the oscillations of the droplet temperature, radius and water concentration induced by the PA process. In Section 3.3 the relative contributions of the heat flux, mass flux and volume change of the particle to the PA signal are discussed.

3.1. Dependence of the photoacoustic signal on droplet radius and relative humidity

The experimental PAA is shown in Fig. 4, top. It was analysed in detail in our previous work [56,49]. Briefly, we observe an increase in the PAA with increasing particle size for all RHs. This was attributed to an increased absorption cross section of the PA laser light of bigger particles. The dependence of the PAA on the RH shows a more complex behaviour. For small particles (0.8–2.1 μm in radius) we observe decreasing PAA signals with increasing relative humidity, while for larger particles (2.6–3.5 μm in radius) the trend is reversed. For the medium sized particles (∼ 2.1–2.6 μm), the PAA shows no particular dependence on relative humidity, as the individual PAA curves largely overlap. These trends were explained in the context of heat and mass flux and their corresponding dependencies on RH and droplet size [56]. In this paper, we further our analysis of the PAA by evaluating the difference in phase between the heat and mass flux components of the PA signal. This was achieved by incorporating the MMS measurements into our single-particle PA measurements. This difference in phase between the heat and mass flux arises from different time constants of the heat transfer and water evaporation/condensation. We were able to retrieve this from a comparison of the experimental PAA data with the theoretical results using mass accommodation coefficients retrieved purely

from MMS [49], which served as an independent probe of our system. In Supplementary Material (Section S2) we present the results of this novel analysis and we find that the PAA can be reduced by up to 10–20% due to the difference in phase between the heat and mass flux, which shows the importance of taking this phase difference into account in the analysis of the PAA.

The corresponding experimental data of the PAP are shown in Fig. 4, bottom. The PAP originates from the finite time delay between the energy absorption and its dissipation into the surrounding air. In the size range considered, the PAP increases with increasing particle radius at all RHs, because larger particles have a higher thermal response time (τ), which results in a slower energy dissipation into the surrounding air and hence in a higher phase delay (Eq. (6)). In the experimentally accessed size range (0.7–3.5 μm), the PAP signal shows an inverse dependence on the RH, i.e. a higher RH speeds up the transfer of energy from the droplet to the surrounding air. The water concentration within a particle increases with increasing RH (Fig. 3) enhancing the energy exchange between the particle and the surrounding air through water evaporation and condensation. As the ratio of the energies dissipated through mass flux to heat flux (f_M) increases, the PA phase delay becomes smaller (see Eq. (6)).

Overall, the PAP proves to be more sensitive to the RH than the PAA. This more pronounced dependence on the mass flux makes the PAP a more sensitive probe for the kinetics of water evaporation and condensation from aerosols. A noteworthy difference between the PAA and PAP data is that the PAP shows a smooth dependence on RH for all particle sizes measured without the reversal of this trend. This highlights the complimentary nature of the two measured quantities and their individual dependencies on droplet size and RH. It is important to note that all PA data acquisitions were performed at 4 kHz. Measurements done on the PA background signal showed that the resonant frequency of the acoustic resonator is 4.068 kHz at low relative humidity (11%) and shifts to 4.084 kHz for high RH (93%). This shift of the resonance frequency with RH alters the PA values measured, however to a minimal extent, well within the experimental error bars. This was confirmed by performing RH-dependent measurements on the background PA signal at 4 kHz and at the actual eigenfrequency of the resonator (not shown).

We have performed simulations of the PA signal as described above, to gain further insight into the dependence of the PAP on droplet radius and RH. The simulations for mixed TEG-water droplets cover the same droplet sizes, RH values, and droplet compositions as our experiments and were performed at the same ambient temperature (Fig. 4). The results for the PAP simulations shown in Fig. 5 describe four different scenarios for the mass flux with different values of the mass accommodation coefficient α_M (Section 2.3). The top left panel of Fig. 5 shows the calculated PAP using the mass accommodation coefficients that were previously retrieved from a fit to the experimental data [49]. In this scenario, α_M depends on particle average temperature, which changes with particle radius, but is independent of the water concentration within the particle with values covering the range α_M from 0.03 to 0.001. The PAP in the top right panel of Fig. 5 was calculated under the assumption that no mass flux takes place (no influence of α_M). The bottom panels show the calculated PAP for constant values of $\alpha_M = 0.001$ on the left and for $\alpha_M = 0.01$ on the right, bracketing the range of the experimental α_M.

It is instructive to start with a discussion of the "no mass flux" simulation (Fig. 5, top right), as this represents the simplest scenario considered. These simulations neglect evaporation and condensation but are otherwise identical to those shown in the top left panel. The comparison helps to disentangle the individual effects of the heat and mass flux on the PAP. Throughout the entire size range (0–4 μm), we observe an increasing PAP with increasing RH, exactly opposite to the trend obtained in the top left panel of Fig. 5 that is in agreement with the one measured experimentally (Fig. 4, bottom). Without mass flux ($f_M = 0$ in Eq. (6)), the dependence of the PAP on the RH is dictated by
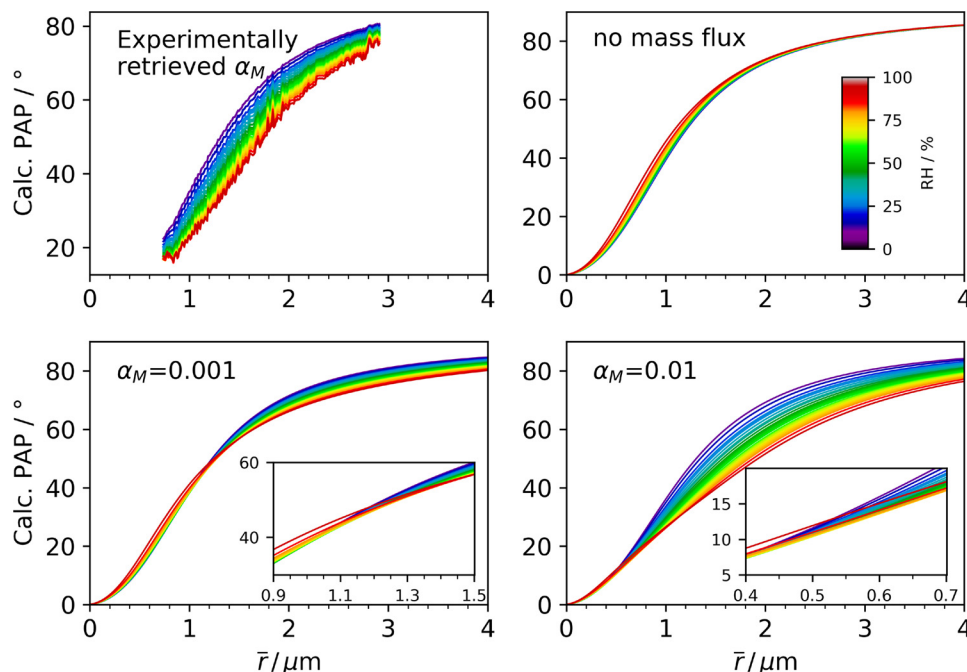
Fig. 5. Calculated PAP as a function of droplet average radius $\bar{r}$ and relative humidity RH for mixed TEG-water droplets at different mass flux conditions: (i) mass flux for varying mass accommodation coefficients as in the experiment (top left) [49], (ii) no mass flux (top right), (iii) mass flux for constant α_M of 0.001 (bottom left), (iv) mass flux for constant α_M of 0.01 (bottom right).

that of thermal response time τ. As the RH increases, so does the water concentration within the particle and as a consequence the heat capacity of the particle increases as well. A higher heat capacity slows down the thermal response of the particle, which results in a large phase delay. From this we can conclude that the RH trends observed experimentally are dominated by the mass flux.

When the mass flux using the α_M from the experiment is considered in the simulations (Fig. 5, top left), the experimental trends of the PAP with relative humidity (Fig. 4, bottom) are indeed well represented by the simulations. These simulations can obviously not be extended beyond the experimentally observed RH and droplet size range for lack of α_M values. In the two bottom traces in Fig. 5, we have instead simulated the PAP assuming constant α_M values. They show a distinct feature, namely a crossing of the individual RH curves. The exact particle size where this crossing occurs, depends on the value of the mass accommodation coefficient. For $\alpha_M = 0.001$ (Fig. 4, bottom left), the crossing appears at $\sim 1.2\,\mu m$. Particles above that size show the same trend as the experimental data, namely a decrease of the PAP with increasing RH. Below the crossing point around $1.2\,\mu m$, the trend switches to that obtained in the "no mass flux" scenario, i.e. an increase of the PAP with increasing RH. Increasing the value of the mass accommodation coefficient to 0.01 (Fig. 4, bottom right), shifts the crossing point of the simulated PAP traces to smaller particle sizes ($\sim 0.5\,\mu m$). The mass flux apparently becomes significant already at smaller particle sizes. This is to be expected since the mass flux contribution to the PA signal depends on the value of α_M. The higher value of α_M in the bottom right panel compared to the bottom left panel also results in a higher sensitivity of the PAP to RH, which is reflected in a bigger spread of the individual PAP curves with RH. We also note that neither the experimental PAP data (Fig. 4, bottom) nor the corresponding simulations (Fig. 5, top left) show any crossing. The simulations for constant α_M (Fig. 5, bottom) indicate that such a crossing might be present in the experiment at droplet sizes smaller than those accessed experimentally. The simulation for $\alpha_M = 0.01$, for example, predicts a crossing at a particle radius of $\sim 0.5\,\mu m$, below the size range of our experiments.

The above results also demonstrate that crossings in the PAA do not necessarily occur at the same droplets radius as crossings in the PAP. In

the experimental PAA data (Fig. 4, top), the crossing region is clearly visible in the size range of 2.1–$2.6\,\mu m$, with no crossing in the PAP at the same size (bottom panel). Such different behaviour of the PAA and PAP could be exploited to optimise the information content when performing PA measurements. Combined PAA and PAP measurements can, for example, be used to retrieve the values of the mass accommodation coefficient [49]. The crossing regions are attractive regions to avoid strong RH biases because the RH dependence is minimal in those regions. This might be important for PA measurements at varying RH, for example during atmospheric measurements.

3.2. Temperature, radius and concentration change during a PA cycle

During a PA cycle, the droplet experiences cyclic perturbations of its temperature, radius, water concentration, and refractive index (as shown in Fig. 1). The MMS measurements (Supplementary Material Section S1) are highly sensitive to droplet size and refractive index changes, and hence can be used to experimentally access these perturbations of the particle equilibrium state. Thereby we were able to identify all key processes which have to be considered in the MMS_A model for a realistic description of the MMS_A experimental data, i.e. temperature-dependent concentration, temperature- and concentration-dependent density, temperature- and concentration-dependent refractive index and mass flux impact on concentration and droplet volume change. Once these key processes were implemented in the model, a good fit of the experimental MMS_A data to the calculated MMS_A data was obtained. From these fits we are now in a position to retrieve experimental values for the amplitudes of oscillation (Fig. 1) in droplet temperature (ΔT), size (Δr) and composition (water concentration ΔC), based on the model presented in Section 2.3 and using the values of α_M from our previous work [49]. To keep the sign information, Δr and ΔC are presented as a difference between the elevated temperature and the average temperature (Fig. 1):

$$\Delta r = r_1 - \bar{r} \tag{13}$$

$$\Delta C = C_1 - \overline{C} \tag{14}$$

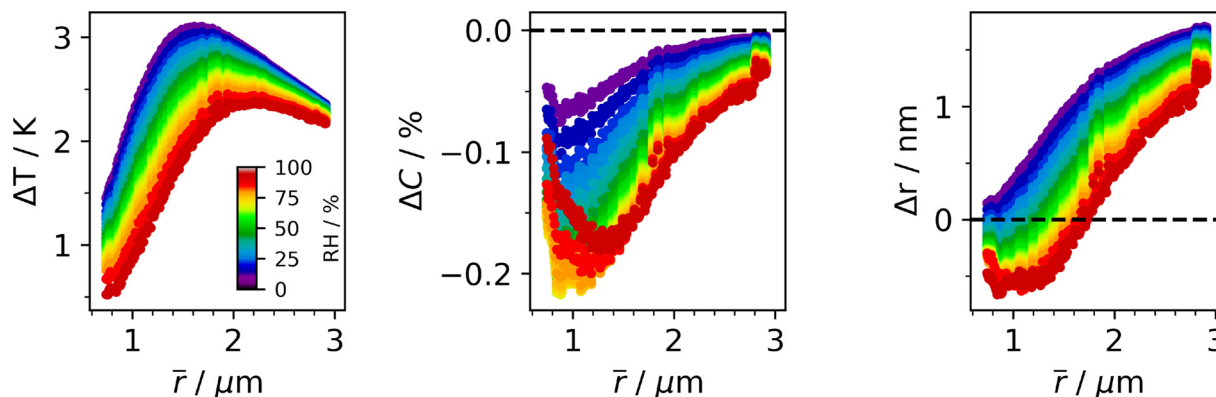Fig. 6 shows the results as a function of droplet size and RH. A

Fig. 6. Amplitude of the temperature ΔT (left) and the water concentration ΔC in % mass (middle) and maximum changes of the droplet radius Δr (right) as a function of droplet average size $\bar{r}$ and RH during a PA cycle.

negative sign for Δr or ΔC indicates that the droplet size or water concentration of the particle at the elevated temperature T_1 are lower than that at the average temperature $\overline{T}$.

The amplitude of the temperature oscillation ΔT (Fig. 6 left) represents the maximum perturbation of the average droplet temperature $\overline{T}$ due to the absorption of the modulated PA laser light. For all droplet sizes, we observe an inverse dependence of ΔT on RH, as a result of two combined effects: (i) higher RH corresponds to higher water concentrations in the droplet, which decreases the absorption cross section of the droplet because water is essentially non-absorbing at the PA laser wavelength of 9.47 μm (see Eq. (1)); (ii) the mass flux, which is more pronounced at higher RH, enhances the heat dissipation, which in turn reduces ΔT. The radial dependence of ΔT at constant RH can also be understood by looking at Eq. (1). The observed increase of ΔT as a function of droplet radius for radii up to ~1.5-2 μm is caused by the increase in the absorption cross section C_{abs} with droplet size. However, for even larger droplets, this increase in C_{abs} is offset by the faster increase of the denominator in Eq. (1), which is not only proportional to $\bar{r}$, but also increases with τ, which in turn increases with the square of the droplet's radius. In total, this leads to a decrease of ΔT for droplets larger than ~1.5-2 μm.

The right panel in Fig. 6 shows that the maximum amplitude of size oscillations Δr lie in the sub-nanometre to nanometre range. Such small changes in particle radius could only be detected because of the high sensitivity of the MMS measurements to the droplet size. The changes in the droplet size during a PA cycle arise from two competing effects: mass flux and heat expansion. At higher temperatures, evaporation of water (mass flux) from the particle's surface results in a decrease of the particle's volume ($\propto r^3$), while heat expansion causes an increase of the particle radius. Since most of the experimental values for Δr are positive (particle size increases with temperature), we can infer for our system that size oscillations are dominated by the heat expansion effect for most particle sizes and RHs. For all droplet sizes, Δr decreases with increasing RH as the increased contribution of the mass flux, and hence increasing water evaporation, effectively cancels out some of the heat expansion. We can also observe (predominantly at high RH and small particle sizes) negative Δr values, which indicates that the mass flux becomes the prevalent effect here. Overall, Δr increases with particle size for all particles, indicating a growing contribution from heat expansion. For particles bigger than ~2 μm, ΔT starts to decrease slightly with increasing radius, while Δr keeps increasing, although less steeply. At first sight, one should expect a decrease of ΔT to translate into a lower Δr, because the heat expansion is reduced. The fact that Δr still increases indicates that the balance between the counteracting contributions of heat expansion and mass flux to the size oscillations favours the former over the latter once ΔT starts to level off and even decrease for the larger particles. This reflects the different temperature dependence of the two contributions: while the heat expansion

decreases linearly with ΔT, the mass flux contribution, whose temperature dependence is governed by the vapour pressure of water, decreases exponentially.

In the course of the PA cycle, the mass flux also alters the particle composition (Eq. (7)). Fig. 6 (middle) displays the amplitude ΔC of the corresponding oscillation in the water concentration, which is out of phase with the temperature oscillation. Water evaporation is more pronounced at higher RH where the mass flux is more important. For all RHs, we observe an increase of $|\Delta C|$ with increasing droplet size for droplets smaller than ~1.2 μm. This can be related to an increased evaporation originating from a strong increase in ΔT. For droplets bigger than ~1.2 μm, $|\Delta C|$ decreases with increasing droplet size for all relative humidities. As described in Ref. [49], α_M of water on TEG surfaces decreases with increasing droplet temperature and thus with increasing droplet radius. This, accompanied by a decrease of ΔT for larger droplets, leads to a decrease in $|\Delta C|$ with increasing droplet size.

The analysis presented above highlights the complementarity of the MMS to the PA measurements. The combined PSPS method is thus a powerful technique for measuring close-to-equilibrium changes of the physical properties of aerosols. Retrieving ΔT, Δr and ΔC allows us to evaluate the corresponding contributions to the PA signal that arise from the heat flux, mass flux and from the change of the droplet volume.

3.3. Contributions to the photoacoustic signal

The PA signal is created through three physical processes – heat flux, mass flux and volume change of the droplet itself. As mentioned previously, the PA laser induces periodic size oscillations at 4 kHz that can be experimentally accessed using MMS (Fig. 6). These size oscillations create a pressure wave in the surrounding air because of the corresponding volume change of the aerosol droplet. This volume change contributes to the PA signal alongside the heat and mass flux. The retrieval of the experimental size change from the MMS measurements allows us now to quantify the volume change contribution to the PA signal.

Fig. 7 shows the various contributions to the PAA as a function of particle size and relative humidity. In these simulations we used the radius dependent average mass accommodation coefficient that changes with particle temperature but is constant throughout all concentrations that we retrieved in our previous work [49]. As the absorption cross section increases with particle radius, so does the heat flux contribution to the PAA (see Eq. (4) and Fig. 7 left). Increasing RH, by contrast, reduces the heat flux contribution as a result of the smaller averaged absorption cross section of wet particles. At larger particle radii the heat flux contribution starts to level off as a consequence of the limiting heat dissipation into the surrounding air [47] that was already evident in the size dependence of ΔT (Fig. 6 left). The mass flux
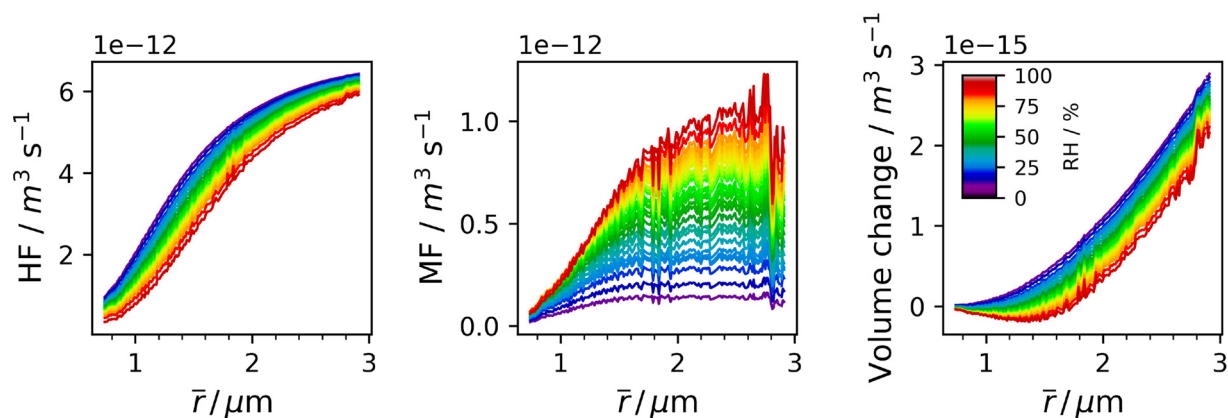
Fig. 7. Calculated PAA contributions from heat flux Q (left), mass flux I (middle) and particle volume change ΔV (right) plotted against average droplet radius $\bar{r}$ at varying relative humidity RH. For the definitions of HF and MF see Eqs. (4) and (5) respectively.

contribution (see Eq. (5)) also increases with increasing particle size (Fig. 7 middle), in line with the ΔT increase and levels off above ~1.6 µm, when ΔT starts to decrease (see above). We also observe that the mass flux contribution increases with increasing RH in line with the higher water content of the particles (see Fig. 3). This behaviour is correlated to that of ΔC. The particle volume change contribution (Fig. 7 right) shows an increase for most particle sizes, which directly follows from the behaviour of Δr (Fig. 6 right). The mass flux is more pronounced at high RH and hence competes more efficiently with the heat expansion and as a result, the volume change of a particle decreases with increasing RH. For particles of 1.5 µm in radius we even observe negative values of ΔV (i.e. out of phase with ΔT) at elevated RH. Under these conditions, the mass flux, rather than heat expansion, governs the volume change of the particle.

The numbers in Fig. 7 illustrate that the heat flux (HF) and mass flux (MF) contributions to the PAA are about ~1000 times higher than the contribution from the droplet volume change. The latter is thus insignificant. Overall, the heat flux represents the largest contribution and hence governs the size-dependence of the PAA measured. However, the PAA trends with RH for larger particles are dictated by the mass flux trends with RH. This is because the increase in the mass flux contribution with RH for large particles overcomes the observed decrease in the heat flux contribution to the PA signal. Furthermore, it is important to note that the heat and mass flux experience a phase shift from one another (shown in Supplementary Material Section S2), which impacts the measured PAA signal. This phase shift is radius and RH-dependent and varies between 0 and 180°, decreasing the PAA signal by ~10%. It is hence important to take this into account when comparing the experimental data with theory.

4. Conclusion

We have presented complimentary photoacoustic (PA) and elastic light scattering studies (modulated Mie scattering, MMS) on single optically trapped aerosol droplets. We have analysed the dependencies of the PA signal on the particle size and the relative humidity, which have long been discussed in the literature. Building on our previous work [56,49] we have analysed the PA phase alongside the PA amplitude, using the MMS as an independent probe of the PA process occurring on aerosol particles. The combination of the PA measurements with MMS measurements provides more detailed insight into the heat and mass flux contributions to the PA signal and into particle size and concentration changes during PA measurements.

In the droplet size range considered, the PA phase shows higher sensitivity to the mass flux than the PA amplitude, making the PA phase a more suitable tool for studies of water transport to and from aerosol particles. Detailed simulations further reveal the influence of the mass

flux and the mass accommodation coefficient on the RH-dependence of the PA phase. In the experimentally accessed droplet size range (0.7–3.5 µm in radius), the PA phase shows a strong decrease with increasing RH. The simulations indicate that this trend could be reversed for droplet sizes below the range accessed experimentally. At constant droplet size, the dependence of the PA amplitude and phase on the relative humidity differ, which provides useful additional information in absorption studies.

Exploiting MMS as an independent probe of the PA signal generation process, we have demonstrated that it is possible to retrieve attolitre volume changes and subnanometre to nanometre size changes of particles. This enabled us to experimentally quantify the individual contributions of heat flux, mass flux and particle volume change to the PA signal emanating from a single trapped particle. We found heat and mass flux contributions to exceed the direct contribution from particle volume change by about a thousand times, so that the latter can be safely neglected. We used tetraethylene glycol as a proxy for organic aerosols that are ubiquitous in the atmosphere. The findings presented in this work represent general trends for such miscible organic aerosols.

Authors' contribution

Matus E. Diveky and Sandra Roy: conceptualisation, methodology, software, formal analysis, investigation, writing – original draft, visualisation. Grégory David: conceptualisation, software, writing – review & editing. Johannes W. Cremer: conceptualisation, methodology, software, writing – review & editing. Ruth Signorell: conceptualisation, methodology, writing – review & editing, supervision, project administration, funding acquisition.

Conflict of interest

None declared.

Appendix A. Supplementary data

Supplementary data associated with this article can be found, in the online version, at https://doi.org/10.1016/j.pacs.2020.100170.

References

[1] R.C. Mesquita, A.M. Mansanares, E.C. da Silva, P.R. Barja, L.C.M. Miranda, H. Vargas, Open photoacoustic cell: applications in plant photosynthesis studies, Instrum. Sci. Technol. 34 (1–2) (2006) 33–58, https://doi.org/10.1080/10739140500373940.

[2] S.F. Corrêa, L. Mota, L.B. Paiva, F.M. do Couto, M.G. da Silva, J.G. de Oliveira, M.S. Sthel, H. Vargas, A. Miklós, Effects of ozone exposure on 'golden' papaya fruit by photoacoustic phase-resolved method: physiological changes associated with carbon dioxide and ethylene emission rates during ripening, J. Appl. Phys. 109 (11) (2011) 114701, https://doi.org/10.1063/1.3592353.

[3] B. Hu, D. Chen, Q. Su, Photoacoustic phase study on the frequency dependence of phase angle and triplet state lifetime of Nd(III)-acetylacetonate, Spectrochim. Acta, Part A 63 (1) (2006) 55–59, https://doi.org/10.1016/j.saa.2005.04.028.

[4] L. Mota, R. Toledo, R. Faria, E. da Silva, H. Vargas, I. Delgadillo-Holtfort, Thermally treated soil clays as ceramic raw materials: characterization by X-ray diffraction, photoacoustic spectroscopy and electron spin resonance, Appl. Clay Sci. 43 (2) (2009) 243–247, https://doi.org/10.1016/j.clay.2008.07.025.

[5] J. Jo, C. Tian, G. Xu, J. Sarazin, E. Schiopu, G. Gandikota, X. Wang, Photoacoustic tomography for human musculoskeletal imaging and inflammatory arthritis detection, Photoacoustics 12 (2018) 82–89, https://doi.org/10.1016/j.pacs.2018.07.004.

[6] I. Steinberg, D.M. Huland, O. Vermesh, H.E. Frostig, W.S. Tummers, S.S. Gambhir, Photoacoustic clinical imaging, Photoacoustics 14 (2019) 77–98, https://doi.org/10.1016/j.pacs.2019.05.001.

[7] H. Moosmüller, R.K. Chakrabarty, W.P. Arnott, Aerosol light absorption and its measurement: a review, J. Quant. Spectrosc. Radiat. Transfer 110 (11) (2009) 844–878, https://doi.org/10.1016/j.jqsrt.2009.02.035.

[8] C. Haisch, Photoacoustic spectroscopy for analytical measurements, Meas. Sci. Technol. 23 (1) (2012) 12001, https://doi.org/10.1088/0957-0233/23/1/012001.

[9] M. Moeckli, C. Hilbes, M. Sigrist, Photoacoustic multicomponent gas analysis using a Levenberg–Marquardt fitting algorithm, Appl. Phys. B 67 (4) (1998) 449–458, https://doi.org/10.1007/s003400050529.

[10] Z. Bozóki, J. Sneider, Z. Gingl, Á. Mohácsi, M. Szakáll, Z. Bor, G. Szabó, A high-sensitivity, near-infrared tunable-diode-laser-based photoacoustic water-vapour-detection system for automated operation, Meas. Sci. Technol. 10 (11) (1999) 999–1003, https://doi.org/10.1088/0957-0233/10/11/304.

[11] V. Altuzar, S. Tomás, O. Zelaya-Angel, F. Sánchez-Sinencio, J. Arriaga, Atmospheric ethene concentrations in Mexico city: indications of strong diurnal and seasonal dependences, Atmos. Environ. 39 (29) (2005) 5219–5225, https://doi.org/10.1016/j.atmosenv.2004.10.002.

[12] H. Yi, R. Maamary, X. Gao, M.W. Sigrist, E. Fertein, W. Chen, Monitoring of nitrous acid (hono) by off-beam quartzenhanced photoacoustic spectroscopy (QEPAS) using external-cavity quantum cascade laser, Imaging and Applied Optics 2016 (2016) JT3A.7, https://doi.org/10.1364/3D.2016.JT3A.7.

[13] M.W. Sigrist, Trace gas monitoring by laser photoacoustic spectroscopy and related techniques (plenary), Rev. Sci. Instrum. 74 (1) (2003) 486–490, https://doi.org/10.1063/1.1512697.

[14] B. Lang, A. Bergmann, Design framework for a gas sensor based on an open photoacoustic resonator, 2016 IEEE SENSORS (2016), https://doi.org/10.1109/icsens.2016.7808433.

[15] S.D. Russo, S. Zhou, A. Zifarelli, P. Patimisco, A. Sampaolo, M. Giglio, D. Iannuzzi, V. Spagnolo, Photoacoustic spectroscopy for gas sensing: a comparison between piezoelectric and interferometric readout in custom quartz tuning forks, Photoacoustics 17 (2020) 100155, https://doi.org/10.1016/j.pacs.2019.100155.

[16] H. Zheng, Y. Liu, H. Lin, B. Liu, X. Gu, D. Li, B. Huang, Y. Wu, L. Dong, W. Zhu, J. Tang, H. Guan, H. Lu, Y. Zhong, J. Fang, Y. Luo, J. Zhang, J. Yu, Z. Chen, F.K. Tittel, Quartz-enhanced photoacoustic spectroscopy employing pilot line manufactured custom tuning forks, Photoacoustics 17 (2020) 100158, https://doi.org/10.1016/j.pacs.2019.100158.

[17] W.P. Arnott, H. Moosmüller, C.F. Rogers, T. Jin, R. Bruch, Photoacoustic spectrometer for measuring light absorption by aerosol: instrument description, Atmos. Environ. 33 (17) (1999) 2845–2852, https://doi.org/10.1016/S1352-2310(98)00361-6.

[18] W.P. Arnott, H. Moosmüller, J.W. Walker, Nitrogen dioxide and kerosene-flame soot calibration of photoacoustic instruments for measurement of light absorption by aerosols, Rev. Sci. Instrum. 71 (12) (2000) 4545–4552, https://doi.org/10.1063/1.1322585.

[19] W.P. Arnott, B. Zielinska, C.F. Rogers, J. Sagebiel, K. Park, J. Chow, H. Moosmüller, J.G. Watson, K. Kelly, D. Wagner, A. Sarofim, J. Lighty, G. Palmer, Evaluation of 1047-nm photoacoustic instruments and photoelectric aerosol sensors in source-sampling of black carbon aerosol and particle-bound PAHs from gasoline and diesel powered vehicles, Environ. Sci. Technol. 39 (14) (2005) 5398–5406, https://doi.org/10.1021/es049595e.

[20] W.P. Arnott, J.W. Walker, H. Moosmüller, R.A. Elleman, H.H. Jonsson, G. Buzorius, W.C. Conant, R.C. Flagan, J.H. Seinfeld, Photoacoustic insight for aerosol light absorption aloft from meteorological aircraft and comparison with particle soot absorption photometer measurements: DOE southern great plains climate research facility and the coastal stratocumulus imposed perturbation experiments, J. Geophys. Res.: Atmos. 111 (D5) (2006), https://doi.org/10.1029/2005d005964.

[21] T. Ajtai, Á. Filep, M. Schnaiter, C. Linke, M. Vragel, Z. Bozóki, G. Szabó, T. Leisner, A novel multi-wavelength photoacoustic spectrometer for the measurement of the UV–vis–NIR spectral absorption coefficient of atmospheric aerosols, J. Aerosol Sci. 41 (11) (2010) 1020–1029, https://doi.org/10.1016/j.jaerosci.2010.07.008.

[22] C. Linke, I. Ibrahim, N. Schleicher, R. Hitzenberger, M.O. Andreae, T. Leisner, M. Schnaiter, A novel single-cavity three-wavelength photoacoustic spectrometer for atmospheric aerosol research, Atmos. Meas. Technol. 9 (11) (2016) 5331–5346, https://doi.org/10.5194/amt-9-5331-2016.

[23] B. Mason, N.L. Wagner, G. Adler, E. Andrews, C.A. Brock, T.D. Gordon, D.A. Lack, A.E. Perring, M.S. Richardson, J.P. Schwarz, M.A. Shook, K.L. Thornhill, L.D. Ziemba, D.M. Murphy, An intercomparison of aerosol absorption measurements conducted during the seac4rs campaign, Aerosol Sci. Technol. 52 (9) (2018) 1012–1027, https://doi.org/10.1080/02786826.2018.1500012.

[24] D.A. Lack, M.S. Richardson, D. Law, J.M. Langridge, C.D. Cappa, R.J. McLaughlin, D.M. Murphy, Aircraft instrument for comprehensive characterization of aerosol optical properties. Part 2. Black and brown carbon absorption and absorption enhancement measured with photo acoustic spectroscopy, Aerosol Sci. Technol. 46 (5) (2012) 555–568, https://doi.org/10.1080/02786826.2011.645955.

[25] C. Haisch, P. Menzenbach, H. Bladt, R. Niessner, A wide spectral range photoacoustic aerosol absorption spectrometer, Anal. Chem. 84 (21) (2012) 8941–8945, https://doi.org/10.1021/ac302194u.

[26] M.I. Cotterell, G.P. Ward, A.P. Hibbins, J.M. Haywood, A. Wilson, J.M. Langridge, Optimizing the performance of aerosol photoacoustic cells using a finite element model. Part 1. Method validation and application to single-resonator multipass cells, Aerosol Sci. Technol. 0 (0) (2019) 1–21, https://doi.org/10.1080/02786826.2019.1650161.

[27] P. Breitegger, M.A. Schriefl, R.T. Nishida, S. Hochgreb, A. Bergmann, Soot mass concentration sensor using quartz-enhanced photoacoustic spectroscopy, Aerosol Sci. Technol. 53 (9) (2019) 971–975, https://doi.org/10.1080/02786826.2019.1635677.

[28] J. Haywood, O. Boucher, Estimates of the direct and indirect radiative forcing due to tropospheric aerosols: a review, Rev. Geophys. 38 (4) (2000) 513–543, https://doi.org/10.1029/1999RG000078.

[29] U. Lohmann, J. Feichter, Global indirect aerosol effects: a review, Atmos. Chem. Phys. 5 (3) (2005) 715–737, https://doi.org/10.5194/acp-5-715-2005.

[30] D. Koch, A.D. Del Genio, Black carbon semi-direct effects on cloud cover: review and synthesis, Atmos. Chem. Phys. 10 (16) (2010) 7685–7696, https://doi.org/10.5194/acp-10-7685-2010.

[31] K.A. Lewis, W.P. Arnott, H. Moosmüller, R.K. Chakrabarty, C.M. Carrico, S.M. Kreidenweis, D.E. Day, W.C. Malm, A. Laskin, J.L. Jimenez, I.M. Ulbrich, J.A. Huffman, T.B. Onasch, A. Trimborn, L. Liu, M.I. Mishchenko, Reduction in biomass burning aerosol light absorption upon humidification: roles of inorganically-induced hygroscopicity, particle collapse, and photoacoustic heat and mass transfer, Atmos. Chem. Phys. 9 (22) (2009) 8949–8966, https://doi.org/10.5194/acp-9-8949-2009.

[32] A. McComiskey, S.E. Schwartz, B. Schmid, H. Guan, E.R. Lewis, P. Ricchiazzi, J.A. Ogren, Direct aerosol forcing: Calculation from observables and sensitivities to inputs, J. Geophys. Res.: Atmos. 113 (D9 may) (2008), https://doi.org/10.1029/2007jd009170.

[33] M. Nirmal, B.O. Dabbousi, M.G. Bawendi, J.J. Macklin, J.K. Trautman, T.D. Harris, L.E. Brus, Fluorescence intermittency in single cadmium selenide nanocrystals, Nature 383 (6603) (1996) 802–804, https://doi.org/10.1038/383802a0.

[34] M.D. King, K.C. Thompson, A.D. Ward, C. Pfrang, B.R. Hughes, Oxidation of biogenic and water-soluble compounds in aqueous and organic aerosol droplets by ozone: a kinetic and product analysis approach using laser Raman tweezers, Faraday Discuss. 137 (2008) 173–192, https://doi.org/10.1039/b702199b.

[35] R. Miles, A. Carruthers, J. Reid, Novel optical techniques for measurements of light extinction, scattering and absorption by single aerosol particles, Laser Photon. Rev. 5 (4) (2011) 534–552, https://doi.org/10.1002/lpor.201000029.

[36] M.I. Cotterell, B.J. Mason, A.E. Carruthers, J.S. Walker, A.J. Orr-Ewing, J.P. Reid, Measurements of the evaporation and hygroscopic response of single fine-mode aerosol particles using a Bessel beam optical trap, Phys. Chem. Chem. Phys. 16 (5) (2014) 2118–2128, https://doi.org/10.1039/c3cp54368d.

[37] G. David, K. Esat, S. Hartweg, J. Cremer, E. Chasovskikh, R. Signorell, Stability of aerosol droplets in Bessel beam optical traps under constant and pulsed external forces, J. Chem. Phys. 142 (15) (2015) 154506, https://doi.org/10.1063/1.4917202.

[38] G. David, K. Esat, I. Ritsch, R. Signorell, Ultraviolet broadband light scattering for optically-trapped submicron-sized aerosol particles, Phys. Chem. Chem. Phys. 18 (7) (2016) 5477–5485, https://doi.org/10.1039/C5CP06940H.

[39] K.J. Knox, J.P. Reid, Ultrasensitive absorption spectroscopy of optically-trapped aerosol droplets, J. Phys. Chem. A 112 (42) (2008) 10439–10441, https://doi.org/10.1021/jp807418g.

[40] M.I. Cotterell, B.J. Mason, T.C. Preston, A.J. Orr-Ewing, J.P. Reid, Optical extinction efficiency measurements on fine and accumulation mode aerosol using single particle cavity ring-down spectroscopy, Phys. Chem. Chem. Phys. 17 (24) (2015) 15843–15856, https://doi.org/10.1039/C5CP00252D.

[41] L. Mitchem, J.P. Reid, Optical manipulation and characterisation of aerosol particles using a single-beam gradient force optical trap, Chem. Soc. Rev. 37 (4) (2008) 756, https://doi.org/10.1039/b609713h.

[42] A. Rafferty, T.C. Preston, Measuring the size and complex refractive index of an aqueous aerosol particle using electromagnetic heating and cavity-enhanced raman scattering, Phys. Chem. Chem. Phys. 20 (25) (2018) 17038–17047, https://doi.org/10.1039/c8cp02966.

[43] R.E. Willoughby, M.I. Cotterell, H. Lin, A.J. Orr-Ewing, J.P. Reid, Measurements of the imaginary component of the refractive index of weakly absorbing single aerosol particles, J. Phys. Chem. A 121 (30) (2017) 5700–5710, https://doi.org/10.1021/acs.jpca.7b05418 PMID: 28691810.

[44] G. David, K. Esat, I. Thanopulos, R. Signorell, Digital holography of optically-trapped aerosol particles, Commun. Chem. 1 (1) (2018), https://doi.org/10.1038/s42004-018-0047-6.

[45] Z. Gong, Y.-L. Pan, G. Videen, C. Wang, Optical trapping and manipulation of single particles in air: principles, technical details, and applications, J, Quant. Spectrosc. Radiat. Transfer 214 (2018) 94–119, https://doi.org/10.1016/j.jqsrt.2018.04.027.

[46] J.W. Cremer, K.M. Thaler, C. Haisch, R. Signorell, Photoacoustics of single laser-trapped nanodroplets for the direct observation of nanofocusing in aerosol photokinetics, Nat. Commun. 7 (2016) 10941, https://doi.org/10.1038/ncomms10941.

[47] J.W. Cremer, P.A. Covert, E.A. Parmentier, R. Signorell, Direct measurement of photoacoustic signal sensitivity to aerosol particle size, J. Phys. Chem. Lett. 8 (14) (2017) 3398–3403, https://doi.org/10.1021/acs.jpclett.7b01288.

[48] P.A. Covert, J.W. Cremer, R. Signorell, Photoacoustic absorption spectroscopy of single optically trapped aerosol droplets, Proc. SPIE, Optical Trapping and Optical Micromanipulation XIV, 1034729 (2017).

[49] S. Roy, M.E. Diveky, R. Signorell, Mass accommodation coefficients of water on organics from complementary photoacoustic and light scattering measurements on laser-trapped droplets, J. Phys. Chem. C 124 (4) (2020) 2481–2489, https://doi.org/10.1021/acs.jpcc.9b09934.

[50] J.M. Haywood, V. Ramaswamy, L.J. Donner, A limited-area-model case study of the effects of sub-grid scale variations in relative humidity and cloud upon the direct radiative forcing of sulfate aerosol, Geophys. Res. Lett. 24 (2) (1997) 143–146, https://doi.org/10.1029/96GL03812.

[51] P. Zieger, R. Fierz-Schmidhauser, E. Weingartner, U. Baltensperger, Effects of relative humidity on aerosol light scattering: results from different european sites, Atmos. Chem. Phys. 13 (21) (2013) 10609–10631, https://doi.org/10.5194/acp-13-10609-2013.

[52] T. Baynard, R.M. Garland, A.R. Ravishankara, M.A. Tolbert, E.R. Lovejoy, Key factors influencing the relative humidity dependence of aerosol light scattering, Geophys. Res. Lett. 33 (6) (2006) L06813, https://doi.org/10.1029/2005GL024898.

[53] W.P. Arnott, H. Moosmüller, P.J. Sheridan, J.A. Ogren, R. Raspet, W.V. Slaton, J.L. Hand, S.M. Kreidenweis, J.L. Collett, Photoacoustic and filter-based ambient aerosol light absorption measurements: instrument comparisons and the role of relative humidity, J. Geophys. Res.: Atmos. 108 (D1) (2003) 4034, https://doi.org/10.1029/2002JD002165.

[54] J.M. Langridge, M.S. Richardson, D.A. Lack, C.A. Brock, D.M. Murphy, Limitations of the photoacoustic technique for aerosol absorption measurement at high relative humidity, Aerosol Sci. Technol. 47 (11) (2013) 1163–1173, https://doi.org/10.1080/02786826.2013.827324.

[55] D.A. Lack, P.K. Quinn, P. Massoli, T.S. Bates, D. Coffman, D.S. Covert, B. Sierau, S. Tucker, T. Baynard, E. Lovejoy, D.M. Murphy, A.R. Ravishankara, Relative humidity dependence of light absorption by mineral dust after long-range atmospheric transport from the Sahara, Geophys. Res. Lett. 36 (24) (2009) L24805, https://doi.org/10.1029/2009GL041002.

[56] M.E. Diveky, S. Roy, J.W. Cremer, G. David, R. Signorell, Assessing relative humidity dependent photoacoustics to retrieve mass accommodation coefficients of single optically trapped aerosol particles, Phys. Chem. Chem. Phys. 21 (2019) 4721–4731, https://doi.org/10.1039/C8CP06980H.

[57] P. Wang, Z. Chen, F. Yang, S. Yang, D. Xing, Intravascular tri-modality system: combined ultrasound, photoacoustic, and elasticity imaging, Appl. Phys. Lett. 113 (25) (2018) 253701, https://doi.org/10.1063/1.5051387.

[58] P. Mohajerani, S. Kellnberger, V. Ntziachristos, Frequency domain optoacoustic tomography using amplitude and phase, Photoacoustics 2 (3) (2014) 111–118 http://www.sciencedirect.com/science/article/pii/S2213597914000184.

[59] T.-C. Ma, M. Munidasa, A. Mandelis, Photoacoustic frequency-domain depth profilometry of surface-layer inhomogeneities: application to laser processed steels, J. Appl. Phys. 71 (12) (1992) 6029–6035, https://doi.org/10.1063/1.350459.

[60] A.J. Campillo, C.J. Dodge, H.-B. Lin, Aerosol particle absorption spectroscopy by photothermal modulation of Mie scattered light, Appl. Opt. 20 (18) (1981) 3100–3103, https://doi.org/10.1364/AO.20.003100.

[61] H.-B. Lin, A.J. Campillo, Photothermal aerosol absorption spectroscopy, Appl. Opt. 24 (3) (1985) 422–433, https://doi.org/10.1364/AO.24.22.

[62] S. Arnold, A.B. Pluchino, Infrared spectrum of a single aerosol particle by photothermal modulation of structure resonances, Appl. Opt. 21 (23) (1982) 41941, https://doi.org/10.1364/ao.21.4194_1.

[63] S. Arnold, E.K. Murphy, G. Sageev, Aerosol particle molecular spectroscopy, Appl. Opt. 24 (7) (1985) 1048–1053, https://doi.org/10.1364/AO.24.001048.

[64] S. Arnold, M. Neuman, A.B. Pluchino, Molecular spectroscopy of a single aerosol particle, Opt. Lett. 9 (1) (1984) 4–6, https://doi.org/10.1364/OL.9.04.

[65] S. Arnold, D.E. Spock, L.M. Folan, Electric-field-modulated light scattering near a morphological resonance of a trapped aerosol particle, Opt. Lett. 15 (20) (1990) 1111–1113, https://doi.org/10.1364/OL.15.001111.

[66] A. Kiraz, Y. Karadag, S.C. Yorulmaz, M. Muradoglu, Reversible photothermal tuning of a salty water microdroplet, Phys. Chem. Chem. Phys. 11 (15) (2009) 2597, https://doi.org/10.1039/b816784b.

[67] H. Vargas, L. Miranda, Photoacoustic and related photothermal techniques, Phys. Rep. 161 (2) (1988) 43–101, https://doi.org/10.1016/0370-1573(88)90100-7.

[68] H.A. Beck, R. Niessner, C. Haisch, Development and characterization of a mobile photoacoustic sensor for on-line soot emission monitoring in diesel exhaust gas, Anal. Bioanal. Chem. 375 (8) (2003) 1136–1143, https://doi.org/10.1007/s00216-003-1810-8.

[69] D.M. Murphy, The effect of water evaporation on photoacoustic signals in transition and molecular flow, Aerosol Sci. Technol. 43 (4) (2009) 356–363, https://doi.org/10.1080/02786820802657392.

[70] R. Raspet, W.V. Slaton, W.P. Arnott, H. Moosmüller, Evaporation-condensation effects on resonant photoacoustics of volatile aerosols, J. Atmos. Ocean. Technol. 20 (5) (2003) 685–695, https://doi.org/10.1175/1520-042620<685:ECEORP>2.0.CO;20032.

[71] O. Iulian, A. Stefaniu, O. Ciocirlan, A. Fedeleş, Refractive index in binary and ternary mixtures with diethylene glycol, 1, 4-dioxane and water between 293.15-313.15k, UPB Sci. Bull. Ser. B: Chem. Mater. Sci. 72 (2010) 37–44.

Matus E. Diveky is a Ph.D. candidate at ETH Zurich, in the Laboratory of Physical Chemistry. He received his M.Sc. degree in Chemistry from University College London. As part of his Master studies he spent a year abroad at University of British Columbia in Vancouver. His current research interests include photoacoustic studies on single aerosols which are optically trapped using lasers.

Dr. Sandra Roy is a postdoctorate fellow at ETH Zurich, in the laboratory of Physical Chemistry. After receiving a BSc at Université Laval (Québec), she proceeded to do her M.Sc. and Ph.D. at the University of Victoria where she studied interfacial structure through a combination of molecular modelling and nonlinear spectroscopy. Her current research interest pertains to single aerosols and surface mass transport studied using photoacoustic spectroscopy.

Dr. Grégory David received his Master and Ph.D. degrees in the field of Aerosol Physics and Chemistry from the University of Lyon 1 in France. During his Ph.D. he worked on using light backscattering to study atmospheric aerosol particles through field and laboratory measurements. Since 2014, he is working at the ETH Zurich as a postdoctoral fellow. His current research activities focus on the use and development of different optical techniques to study fundamental processes in submicron-sized aerosol particles. This includes optical trapping, phase transitions, hygroscopic growth, evaporation and photochemistry.

Dr. Johannes W. Cremer obtained his Ph.D. at laboratory of Physical Chemistry of ETH Zürich, where he also received his BSc and MSc degree in Interdisciplinary sciences. His Ph.D. work included the establishment of a single-particle photoacoustic instrument for absorption studies. He is currently a postdoctoral fellow at Harvard University developing a quantum spin sensor for microscopic nuclear magnetic resonance measurements.

Dr. Ruth Signorell received her M.Sc. and Ph.D. degrees in the field of molecular spectroscopy from the Swiss Federal Institute of Technology (ETH). She started her aerosol research in 2002 as an Assistant Professor at the Georg-August University Goettingen, Germany. Between 2005 and 2012, she was first Associate Professor and later Full Professor at the University of British Columbia in Vancouver, Canada. In 2012, she returned to Switzerland to take up a position as a Full Professor for Physical Chemistry in the Department of Chemistry and Applied Biosciences at ETH Zuerich. Her research interests focus on spectroscopic studies of fundamental processes in aerosol particles and molecular clusters. Her research group introduced the first single-particle photoacoustic instrument for the study of aerosol particles that isolated in air by optical traps.